Author/s:
Akinoglu, GE;Patchett, L;James, TD;Mulvaney, P;Hutchison, JA

Title:
Dual Resonant Plasmonic Infrared Pixels for Selective Optical Encoding

Date:
2025-09-18

Citation:
Akinoglu, G. E., Patchett, L., James, T. D., Mulvaney, P. & Hutchison, J. A. (2025). Dual Resonant Plasmonic Infrared Pixels for Selective Optical Encoding. Advanced Materials Technologies, 10 (18), https://doi.org/10.1002/admt.202500035.

Persistent Link:
https://hdl.handle.net/11343/362650

ADVANCED MATERIALS TECHNOLOGIES
www.advmattechnol.de

Dual Resonant Plasmonic Infrared Pixels for Selective Optical Encoding

Goekalp Engin Akinoglu, Leshy Patchett, Timothy Denis James, Paul Mulvaney, and James Andell Hutchison**

Plasmonic metasurfaces allow the optical encoding of information based on bright and non-fading colors with a resolution at the diffraction limit. The optical information is encoded by varying the dimensional parameters of the plasmonic nanostructures, which are then clustered into nanopixels that are parallel and spectrally addressable. The storage density can be further increased by employing asymmetric and polarization-dependent nanostructures. However, further increases in storage density and security capabilities are still vital for the successful implementation of plasmonic metasurfaces as encoding and encryption solutions. Recent progress in infrared hyperspectral imaging has opened up the possibility of covert image encoding. Here, the optical properties of double resonant plasmonic nanostructures are investigated in the mid-infrared. The structures consist of plasmonic nano-antennas that are placed inside resonant plasmonic ring cavities. The associated plasmonic resonances weakly interact, which causes hybridization. However, it is shown that the plasmonic resonances can be nearly independently tuned if the optimal geometry is used and discuss selective and simultaneous optical encoding in mid-wavelength and long-wavelength infrared regions.

1. Introduction

In ancient Rome, gold nanoparticles were utilized to color glass and ceramics, resulting in artwork that has been preserved for centuries.[1] Their color is based on the collective oscillations of electrons in the gold nanoparticles, known as localized surface plasmons.[2] Unlike dyes or pigments, plasmonic nanoparticles are chemically and thermally stable and incapable of photobleaching. The color can be tuned by adjusting the plasmon excitation energy, which is influenced by the size, shape, and arrangement of the nanoparticles.[2]

In recent years, advanced plasmonic metasurfaces have been developed, creating plasmonic mosaics consisting of nanopixels with geometric dimensions below the diffraction limit.[3–6] These plasmonic mosaics have several promising applications in optical data storage and security, whereby the stored optical information can be read out with high-resolution optical microscopy.[3–6] Furthermore, nanophotonic pixels have been utilized in applications such as sensing,[7] ultra-compact camera pixels,[8] and for hyperspectral imaging.[9–11] Of note is the development of multi-resonant pixels, which allow multiple layers of information to be patterned onto the same target area, increasing the potential information storage density and security via spectral filtering. Recently, covert imaging was demonstrated using plasmonic apertures with tunable resonances in the infrared.[12,13] Another promising approach is the use of structures or assemblies which exhibit tunable dual plasmon resonances. Polarization dependent, dual resonant pixels have been developed using plasmonic structures such as gold nanorods[14] and coupled gold nanoparticle oligomers.[15] However, in these cases, while readout may be enabled through a combination of spectral and polarization filters, independent tuning of each resonance is often convoluted and challenging. For example, in the case of nanorods, both the transverse and longitudinal plasmon modes are shifted when the rod's aspect ratio is changed. The use of asymmetric cross-shaped apertures offers a promising alternative, where each arm can be addressed independently due to geometrically orthogonal plasmon modes.[16,17] Alternatively, two or more uncoupled or weakly coupled plasmonic structures may be incorporated into a single diffraction limited pixel, which forms the basis for this work. Here, we investigate IR, dual-resonant plasmonic pixels based on antennas placed inside ring cavities.

As an initial model system, we first consider concentric disk-ring cavities (CDRCs). CDRCs have been thoroughly

G. E. Akinoglu, L. Patchett, P. Mulvaney, J. A. Hutchison
ARC Centre of Excellence in Exciton Science
School of Chemistry
University of Melbourne
Parkville, VIC 3010, Australia
E-mail: engina@zedat.fu-berlin.de; james.hutchison@unimelb.edu.au
T. D. James
Reserve Bank of Australia
Craigieburn, VIC 3064, Australia

The ORCID identification number(s) for the author(s) of this article can be found under https://doi.org/10.1002/admt.202500035

DOI: 10.1002/admt.202500035

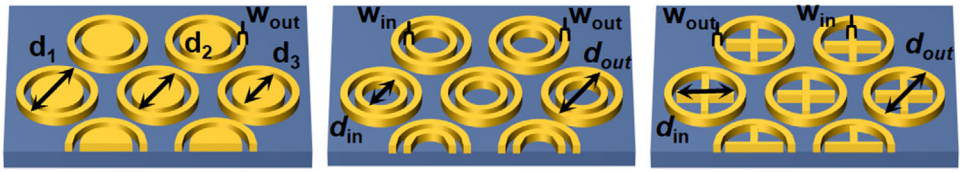

Scheme 1. Dual resonant plasmonic arrays formed by embedding gold disks, rings, or crosses within gold rings. For the concentric disk-ring cavities (CDRCs), d_1 denotes the outer ring diameter, d_2 the inner ring diameter, and d_3 disk diameter. For concentric ring-ring configurations (CRRCs), d_{in} refers to the inner central ring diameter, while d_{out} represents the outer central ring diameter. For the concentric cross-ring cavities (CCRCs), d_{in} specifies the cross length, and d_{out} defines the outer centric ring diameter. The widths of the rings and crosses are described by $w_{out} = w_{in}$, the pitches by p and the thicknesses by t.

investigated in the visible spectrum and their optical properties are determined by the complex interplay between the individual responses and interactions of the rings and disks.[18,19] The plasmonic excitation energies and their interactions are heavily influenced by the geometrical parameters of the CDRCs. Typically, the plasmon resonance excitation energy experiences a redshift with increasing size. However, for small inter-particle distances, resonance hybridization produces bonding and antibonding modes with shifted excitation energies.[18,19] Furthermore, in the case of CDRCs Fano resonances can be observed due to the coupling of the bright dipolar resonance of the disks to the dark multipolar resonances of the rings.[18,19] The reduced line shape of these Fano resonances enables a high refractive index sensitivity that has attracted intense interest as an approach to biosensing.[20] However, both coupling mechanisms are governed by near-field interactions and this limits selective control of the individual plasmon excitations associated with the respective disks and rings. In this study, we investigate the plasmon resonances of different antenna designs placed within rings and demonstrate that their plasmon excitation energies can be independently optimised and varied in a programmable and predictable fashion to meet the needs for ultra dense covert optical encoding.

2. Results

We consider in our simulations the spectral range between 1000 and 7000 wavenumbers (1.4–10.0 micron wavelength), spanning the near and mid-IR regions. The plasmonic antennas are placed in a hexagonal arrangement to increase the overall density of the plasmonic resonators. Our initial model system comprises CDRCs, as illustrated in **Scheme 1**. The system features three critical parameters that dictate its complex plasmonic response: the radii of the disks d_1, the inner radii of the rings d_2, and the outer radii of the rings d_3. We begin by exploring the effect of varying the rings' outer radius while keeping the inner radii of the rings and the radii of the disks constant (as shown in **Figure 1**A). The CDRCs are represented by solid lines, while the reflectance spectra of the isolated rings and disks are shown as dashed and short-dashed lines, respectively. Across all parameters, we observe that the plasmon excitation for the rings occurs at around 2000 cm^{-1}, while for the disks, it occurs at around 4500 cm^{-1}. As the width of the individual rings increases, we note a rise in the resonance broadening, which is also evident in the respective CDRCs. Increasing the width of the plasmonic ring enhances scattering losses as more material interacts with the electromagnetic field, leading to increased dispersion and energy loss.

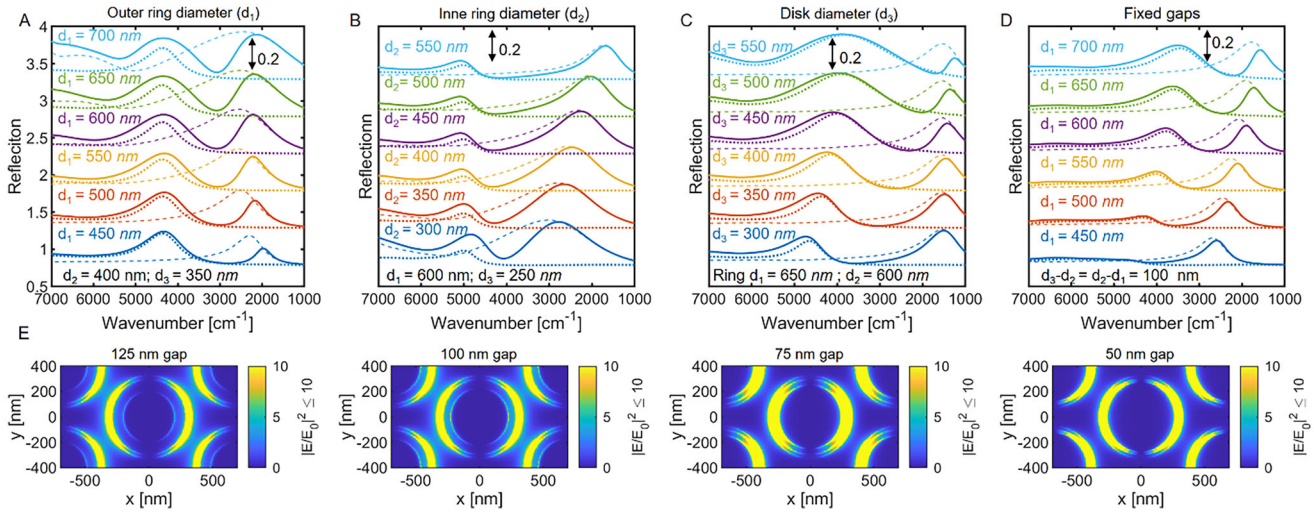

Figure 1. Reflectance spectra of ring-disk resonators with different geometries. Solid lines: ring-disk resonators; short, dashed lines: spectra of the isolated disks; long dashed lines: spectra of the isolated rings. Reflectance for different outer ring diameter A), different inner ring diameter B), disk diameter C), and fixed radii relationship: w = r1 − r2 = r2 − r3 = 50 nm D). xy-electric near-field cross sections for different degrees of hybridization between the disks and rings E).

Simultaneously, the increased material volume enhances intrinsic losses, as more electron collisions (ohmic losses) occur within the metal, absorbing more energy. These combined effects of surface scattering and intrinsic losses dissipate energy more rapidly, leading to broader resonance peaks and reduced sharpness in the spectral response.

Further, as the ring plasmon resonance broadens, it overlaps with that of the disks, resulting in the hybridization of the plasmonic modes.[18,19,21] The resonance widths of the bonding modes, which are slightly red-shifted compared to their ring parent modes, are also drastically reduced. Contrary to this, the resonance widths of the anti-bonding modes, which are slightly blue-shifted to the disk parent modes, are increased.

Next, we investigate the effect of the inner ring radius while keeping the outer ring radius and the diameter of the inner disk fixed (**Figure** 1B). By varying the inner ring diameter and decreasing the ring width, we observe a corresponding redshift of the plasmon resonance excitation energy of the bonding mode and its parent ring mode. We also observe a reduction in the broadening of the bonding and parent modes. Therefore, the value of the inner ring diameter is critical for tuning the plasmon resonance and maximizing its quality factor. Conversely, we notice only minor changes in the excitation energies of the anti-bonding modes. For small inner ring diameters, where the plasmon resonances of the ring and disk overlap, we observe changes in the resonance width of both the bonding and anti-bonding modes, similar to our previous results.

Furthermore, we investigate the impact of disk size on the dual resonance of the CDRCs (**Figure** 1C). As we increase the disk diameter, we observe a red-shift in the plasmon resonance of the anti-bonding mode and its disk parent mode. However, we also note a substantial broadening of their linewidths. The increase is attributed to increased radiative losses and scattering.[22] This is undesirable, as high Q-factors are essential for optical encoding and other applications, including refractive index sensing[20] or increased light-matter interactions.[23]

In **Figure** 1D, we investigated the reflectance of rings with fixed ring widths and gap sizes between the inner disks and the outer rings. We kept the ring width fixed at 50 nm since previous results have suggested that smaller ring widths can drastically increase the quality factor of their resonances. With increasing size, we observed a redshift in the plasmon excitation energies of both the rings and disks, as well as their hybridized modes. Notably, the resonance widths of the bonding modes and their parent ring modes remained small even for larger ring diameters, confirming the hypothesis that rings are a suitable design choice for dual resonant plasmonic templates. However, the anti-bonding mode and its parent disk resonances exhibited a low quality factor compared to the circumferential rings. The large disk resonance width leads to increased spectral overlap with the plasmonic ring modes and enhanced hybridization. It is worth noting that the challenge for dual plasmonic resonators is to reduce this plasmonic hybridization mediated by their electric near-field interactions, as illustrated in **Figure** 1E. As a result, we conclude that CDRCs are not an ideal platform for achieving selective dual resonance control due to the sizable energy dissipation of the plasmonic disk cavities inside the rings.

Hence, we have explored two alternative geometries (see also **Scheme** 1). Since the outer rings exhibit good quality factors for small widths, it is reasonable to hypothesize that replacing the disks with inner rings could yield superior optical performance. To investigate this, we measured the dual resonance excitation of centric ring-ring cavities (CRRCs). For these measurements, we fixed the outer mean ring diameters and varied the mean inner ring diameters (**Figure** 2A). We observed that the excitation energy of the bonding mode remained relatively constant at 1483 cm^{-1} ± 51 cm^{-1} for different mean inner ring diameters. Furthermore, the rings displayed an excellent linear relationship between the mean ring diameter and the corresponding parameters (see **Figure** 2A2).

Subsequently, we fixed the inner ring diameter and varied the outer ring diameter (see **Figure** 2B). For gaps smaller than 100 nm between the outer and inner rings, the rings hybridized with a corresponding shift in the bonding and anti-bonding modes. However, for larger outer rings with gaps above 100 nm, we observed a remarkably linear relationship between the excitation energy and the mean diameter with a root mean square error (RMSE) of 11 cm^{-1} (see **Figure** 2B2). These findings indicate a high degree of control over the plasmonic excitation energies of the outer rings, while the inner rings exhibit a more considerable margin of error. This limitation suggests that, in practical applications, the inner ring excitation energies cannot be too closely spaced as they would become indistinguishable. Additionally, a significant challenge is posed by the requirement of a relatively large gap of over 100 nm between the rings in order to achieve selective resonance control. This gap can be attributed, at least in part, to the bilobate nature of the ring cavities, which results in a relatively large interaction space for plasmonic hybridization.

Hence, we next investigate anisotropic-shaped structures and incorporated crosses within the ring cavities. As shown in **Figure** 2C, the use of inner crosses results in a reduction in both the spatial electric field and spectral overlap, reducing plasmon hybridization to the outer ring. We note further advantages of a polarization-dependent optical response, where the resonance energy of each polarization axis could be tailored by adjusting the size of the corresponding aligned bars. As shown in **Figure** 2C, the high energy resonances of the centrical cross-ring cavities (CCRCs) can be excellently controlled by the size of the crosses while keeping the center diameters of the outer rings fixed. The RMSE of 127 cm^{-1} is superior to that of CRRCs.

Finally, we explore the effect of the outer ring diameter on the resonances (**Figure** 2D). Once again, an excellent linear relationship between the outer ring excitation energy and the ring diameter is observed. However, in contrast to CCRCs or CDRCs, the inner cross cavities can be positioned approximately 50 nm from the outer rings before plasmonic hybridization shifts the modes. In our specific case, the spectral range between 3250 cm^{-1} and 2250 cm^{-1} acts as a stop zone, preventing the hybridization of the plasmonic resonances. If the inner crosses are too large or the outer rings are too small, the resonance is inside the stop zone, leading to distortion of the plasmonic excitation energies. Given the smaller RMSE of the outer rings compared to the inner crosses, the ring resonances can be spaced more densely than that of the inner cross antennas. As a result, the stop zone should be asymmetrically placed towards lower energies to optimize performance.

Overall, for both CCRCs and CRRCs, the outer ring excitation energy can be more precisely and reliably controlled than that of

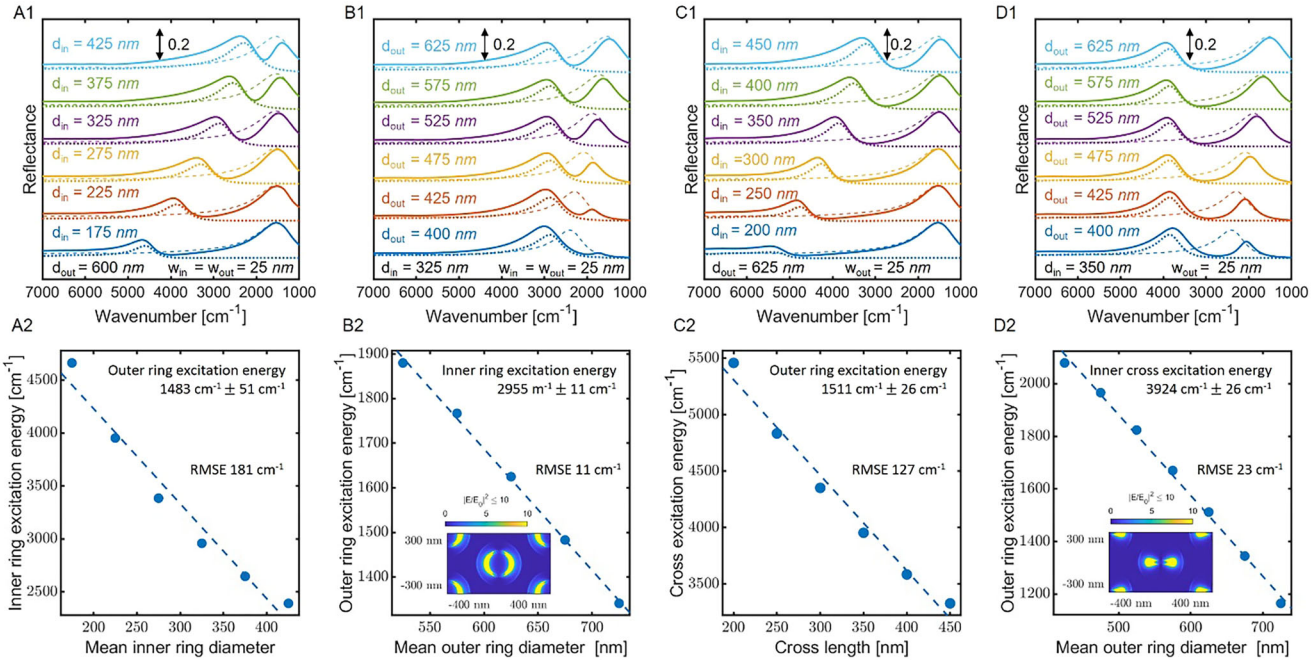

Figure 2. Reflectance spectra of Outer Ring - Inner ring/cross resonators for different geometries. Solid lines: Outer ring - Inner ring/cross resonators; short, dashed lines: respective Inner rings/crosses alone; long dashed lines: respective outer rings alone. The widths of the rings are kept at 25 nm. Reflectance spectra for varying mean inner ring diameters and fixed mean outer ring diameters A1) and linear fit of the inner ring excitation energies A2). Reflectance spectra for fixed mean inner ring diameters and varying outer ring diameters B1) and linear fit of the outer ring excitation energy B2). Reflectance spectra for varying cross lengths and fixed mean outer ring diameters C1) and linear fit of the cross-excitation energies C2). Reflectance spectra for fixed cross lengths and varying outer ring diameters D1) and linear fit of the outer ring excitation energy D2). The inset in Figure B2 and D2 shows a typical electric near field cross sections of ring-ring and cross-ring resonators.

the inner structures, as indicated by the lower simulated RMSE values (11 cm^{-1} for the outer ring in CCRCs and 23 cm^{-1} in CR-RCs, compared to 182 cm^{-1} for the inner cross and 127 cm^{-1} for the inner ring, respectively). This makes the outer ring resonance the more robust component for deterministic spectral encoding.

For completeness, we extend our investigation to explore the effects of pitch and film thickness. As shown in **Figure 3**A, the resonance position remains unchanged as the feature pitch is increased, confirming that the surface plasmon resonance is independent of grating coupling or lattice resonance.[24] However, the intensity of the reflection peak decreases as the pitch increases. This reduction can be attributed to the decreased areal density of plasmonic cavities with increasing pitch length, which weakens the overall resonant response.

In contrast, the film thickness significantly influences the surface plasmon resonance energy. As seen in **Figure 3**B, increasing the film thickness leads to a noticeable redshift in the surface plasmon resonance peak wavelength.[25] This shift arises

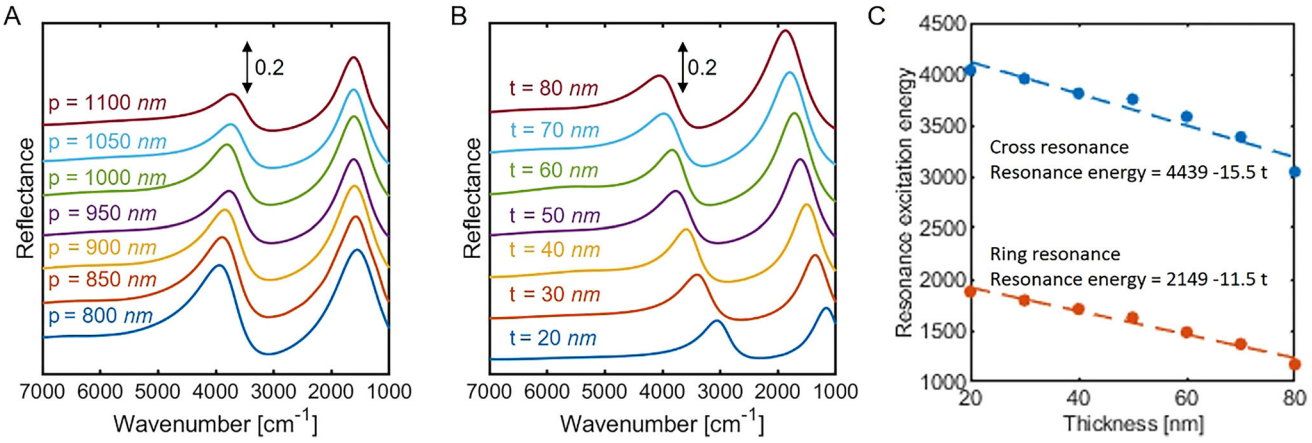

Figure 3. Reflectance spectra of the CCRCs for different pitches for varying pitch size p A) and varying metal thickness t B). The cross length was fixed at 350 nm, the ring diameter was fixed at 625 nm and the width of the plasmonic cavities was fixed at 50 nm.

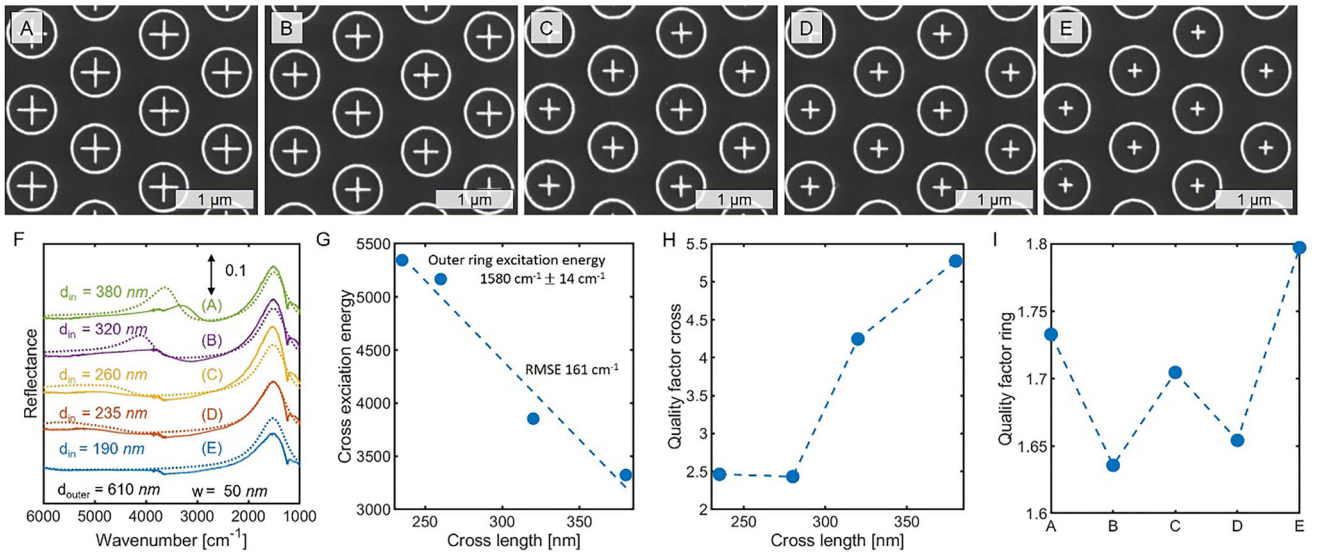

Figure 4. Experimental results on ring/cross resonators with a constant mean ring diameter of 610 nm. SEM images with cross arm lengths of 380 nm A), 320 nm B), 260 nm C), 235 nm D), 190 nm E). The experimental IR reflectance spectra is shown in F), with corresponding linear fit for cross resonance energy G), quality factor of the cross H) and quality factor of the ring I).

from changes in the vertical confinement of the plasmonic mode: as the metal becomes thicker, the electromagnetic fields extend deeper into the structure, reducing their confinement near the metal–dielectric interface. This broader field distribution lowers the restoring force acting on the oscillating surface charges, resulting in a reduced resonance energy and a shift to longer wavelengths. In our configuration, where the metal slabs are placed in air on top of a high-index silicon substrate, the asymmetry of the surrounding dielectric environment further influences the resonance behavior, but the redshift is primarily driven by the increased thickness of the metal.

In **Figure** 3C, both the cross- and ring-resonances show a nearly linear dependence on film thickness. However, the cross-resonance exhibits a ≈35% larger shift, indicating greater sensitivity to vertical geometry changes. This enhanced response results from its smaller overall size and more confined field distribution, which make it more responsive to variations in the vertical mode profile. This suggests that while both resonances respond predictably to changes, the cross-resonance is more sensitive to variations in film thickness. This strong thickness dependence makes simple analytical solutions challenging, although the dispersion of surface plasmon resonances in the infrared can follow the light line, and simple mathematical descriptions have been demonstrated to be precise for plasmonic whispering gallery modes in the infrared.[23,26]

The stronger thickness dependence of the cross-resonance allows an additional degree of tunability, which may be useful for spectral adjustment. However, this also means that small variations in film thickness during fabrication can lead to slightly larger shifts in the cross-resonance compared to the ring, which may be relevant for applications requiring high spectral stability. Nonetheless, within the typical fabrication range of 20–100 nm, these variations remain limited, and the lateral dimensions of the structures remain the dominant factor in determining the optical response. Film thickness thus serves primarily as a secondary tuning parameter for fine control.

Finally, we experimentally validated the computational results. CCRC cavities were fabricated using electron beam lithography on undoped silicon, with each configuration patterned over a 150 × 150 μm area. We maintained a constant outer ring diameter in the first series while varying the cross diameter (**Figure** 4A–E). The reflectance spectra revealed two distinct reflection maxima, corresponding to the cross resonance and the ring resonance. Additionally, water vapor absorption peaks were observed around 3700–3100 cm^{-1}, corresponding to the O-H stretching mode, and around 1900–1500 cm^{-1}, corresponding to the H-O-H bending vibration. Moreover, the Fuchs-Kliewer surface phonon modes of the native SiO_2 layer appeared in the wavenumber range of 1100 to 1300 cm^{-1}, corresponding to the Si-O stretching vibrations.

The experimental and computational results agree strongly (**Figure** 4F). The computational results were normalized to facilitate a more accurate comparison. Both the ring resonance excitation energy and peak width show excellent agreement between experimental measurements and FDTD simulations.

However, the comparisons between experiment and simulation for the cross resonance are less precise. We note a marked broadening and lower intensity observed in the experimental results. Simulations were performed with polarized light; depending on whether it's aligned with the arms of the cross (either along the horizontal or vertical axes), the electric field couples more effectively to the plasmonic modes. This can enhance or suppress the plasmonic resonance, leading to more efficient light absorption and, thus, lower reflectance peaks. However, experimental results were performed with unpolarized light. Likewise, **Figure** 3B suggests that the cross resonance is extremely sensitive to small variations in metal thickness. Hence minor anisotropy during metal deposition could potentially contribute to the experimentally observed broadening effect.

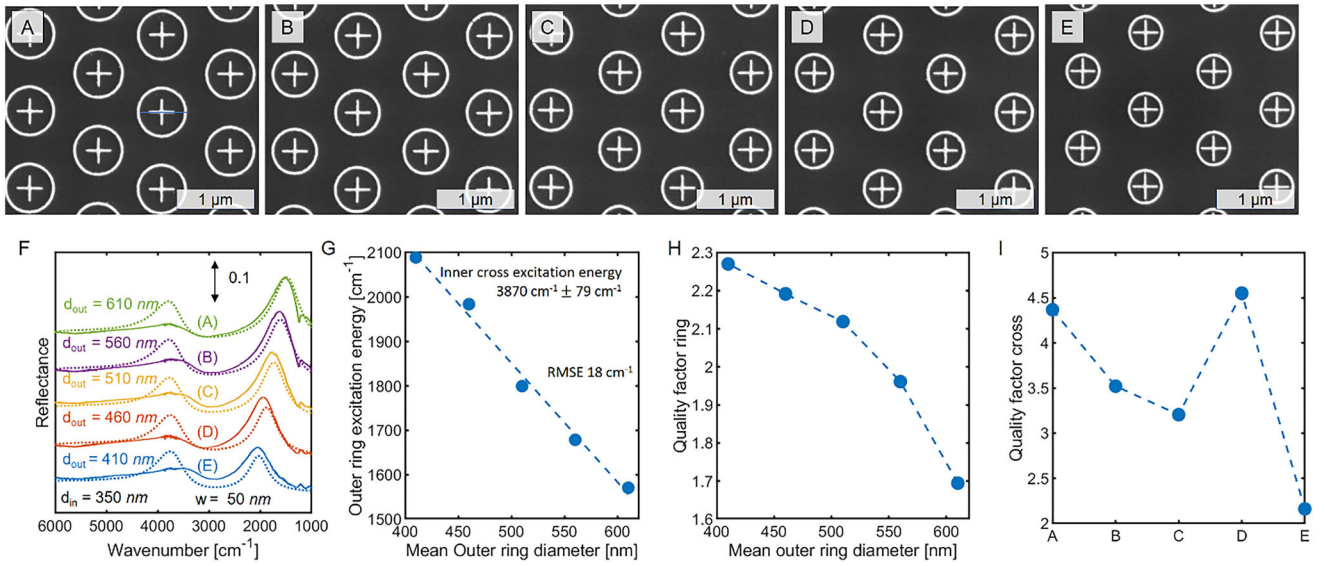

Figure 5. Experimental results for ring/cross resonators where the cross length is kept constant. SEM images of crosses with lengths of 610 nm A), 560 nm B), 510 nm C), 460 nm D), 410 nm E). The experimental IR reflectance spectra are shown in F), with corresponding linear fits for the ring resonance energy G), quality factor of the ring H), and quality factor of the cross I).

The experimental results demonstrate a clear linear trend between the cross-arm length and its resonance excitation energy. However, the root mean square error (RMSE) is relatively high at 161 cm^{-1}, indicating significant measurement variability. In contrast, the ring resonance exhibits much less fluctuation, with a relative standard deviation of only 18 cm^{-1}, suggesting a more stable and reproducible resonance behavior.

The quality factor (Q-factor) increases with larger cross structures, indicating improved resonance sharpness and reduced energy dissipation. For the smallest cross, however, we were unable to clearly identify the resonance peak, likely due to the weak coupling of the plasmonic modes or broader spectral features that obscure the peak (Figure 4H). In comparison, the quality factor of the ring resonance is consistently lower than that of the crosses (Figure 4I), which may be attributed to the different geometrical confinement and plasmonic mode coupling in the ring structure but also by the lower excitation energy.

In the second series of experiments, we kept the cross diameter constant while varying the outer ring diameter (**Figure 5**A–E). Similar to the first series, two primary reflection maxima were observed in the reflectance spectra, corresponding to the cross resonance and the ring resonance (**Figure 5**F).

As expected from the computational models, increasing the ring diameter resulted in a redshift of the ring resonance, with the resonance energy shifting to lower values. Moreover, a clear linear correlation was observed between the ring diameter and the resonance excitation energy (Figure 5G). This behavior further validates the predictive accuracy of the computational models for both the cross and ring resonances.

The second series demonstrated a significant improvement in RMSE, leading to a more accurate determination of the cross and ring resonances than the first series. Notably, the determination of the outer ring resonance proved much more precise than the cross resonance, further highlighting the robustness of the ring's plasmonic behavior.

As shown in Figure 5H, the experimental Q-factor of the ring resonance decreases with increasing ring diameter, even though the full width at half maximum (FWHM) remains nearly constant. This behavior can be understood by recalling that the Q-factor is defined as $Q = \tilde{\nu}_0/\Delta\tilde{\nu}$, where $\tilde{\nu}$ is the resonance wavelength and $\Delta\tilde{\nu}$ is the FWHM. Since the resonance wavelength redshifts with increasing ring size, while the FWHM does not change significantly, the Q-factor naturally decreases. This suggests that energy dissipation is more prominent in larger rings despite the consistent spectral width of the resonance peak.

On the other hand, the cross-resonance Q-factor remained relatively stable and showed little dependence on the ring diameter, reflecting the weaker coupling of the cross structure's plasmonic modes to external fields in this configuration (Figure 5I). This stability underscores the robustness of the cross resonance, but also its limitation in terms of fine-tuning compared to the ring resonance.

3. Discussion

Modern hyperspectral infrared cameras cover a much narrower spectral range than traditional FTIR systems but enable parallel data acquisition across entire scenes, significantly improving imaging speed and throughput. For instance, the Telops (Quebec City, Canada) hyperspectral camera series offers capabilities in the short-wavelength infrared (SWIR) to mid-wavelength infrared (MWIR) regions, with a spectral range from 1.5 μm (6,666 cm^{-1}) to 5.4 μm (1,851 cm^{-1}). It also offers long-wavelength infrared (LWIR) capabilities, covering the range from 7.4 μm (1,351 cm^{-1}) to 12.5 μm (800 cm^{-1}).

The spectral region between 5.4 μm and 7.4 μm, often referred to as the "non-atmospheric window," is typically blocked due to the strong absorption and emission by water vapor, which can oversaturate the cameras. As a result, the infrared spectrum is divided into two distinct regions.

Our optical plasmonic design leverages this limitation by enabling simultaneous optical encoding across the combined SWIR and MWIR regions, as well as the LWIR region. Interestingly, the inaccessible portion of the non-atmospheric window can coincide with the plasmon hybridization stop zone, which spans about 1,000 wavenumbers. From the experimental data of the CRCCs, we determined that the standard error for the outer ring resonance spanning the LWIR is 18 wavenumbers. As a result, for a spectral region spanning 550 wavenumbers, we can encode approximately 15 distinguishable data points.

In the combined SWIR and MWIR region, with a selected range from 6,666 cm^{-1} to 2,350 cm^{-1}, the experimental error margin is broader at 161 wavenumbers. Despite the more considerable uncertainty, this more extensive range enables us to encode around 13 distinct data points across this spectral span.

Therefore, we could potentially have a total of 195 points, which is nearly equivalent to 8-bit data—the standard used for storing grayscale images in modern visual displays. However, the data storage capacity can be further increased, potentially doubled or quadrupled, by incorporating polarization-sensitive elements, such as asymmetric crosses for the combined SWIR and MWIR region or polarization-sensitive split-ring resonators designed for the LWIR resonance.

Plasmonic meta-pixels can be fabricated at scales below the diffraction limit, and our results demonstrate that the resonances in CDRCs are highly localized, with negligible influence from far-field diffraction or lattice couplings. As a result, in an ideal scenario with diffraction-limited readout, the minimum achievable pixel size would be 12.5 μm × 12.5 μm, yielding 124.8 million data points. This number could be further amplified by leveraging polarization-sensitive plasmonic designs (see **Figure** S1, Supporting Information).[17] However, the primary constraint on resolution remains the optical readout system. A typical LWIR hyperspectral camera's pixel pitch size is 30 μm, which is close to the maximum wavelength it is designed to detect. Despite having lower storage capacity than current optical storage technology, covert optical encoding and selective manipulation of infrared light is particular promising for multispectral solutions for security, defence and beyond.[27]

4. Conclusion

The dual resonance behavior of plasmonic structures, including disks, rings, and cross-shaped elements, was explored. A key aspect of achieving selective control of the plasmon excitation resonance was to reduce the plasmonic coupling governed by near-field interactions. We found that CDRCs are unsuitable due to the broad resonance of the inner disk cavities, especially as their diameter increases, which leads to significant hybridization with the outer ring modes. CRRCs with small ring widths showed satisfactory performance and already evinced selective resonance tunability. We demonstrated a linear relationship between the size of the inner and outer disks and their two resonances for an appropriate range of geometrical parameters. However, the bilobate nature of CRRCs and extensive near-field interaction requires a large gap between the rings. The best performance was achieved with CCRCs. Overall, our study demonstrates the successful design of dual resonant plasmonic pixels with selective resonances in the mid-infrared range optimized and varied in a programmable and predictable fashion to meet the needs for simultaneous and selective ultra-dense covert optical encoding for both the combined SWIR and MWIR, as well as the LWIR region.

5. Experimental Section

Experimental: Undoped silicon substrates were thoroughly cleaned by soaking in acetone for 5 minutes, followed by isopropanol (IPA) and deionized (DI) water each for 15 seconds. The substrates were immediately dried, baked at 180°C for 20 minutes to remove excess water, and allowed to cool to room temperature. For the exposure, a bilayer resist process was used. First, a sacrificial 495 k molecular weight A3 (3% in anisole) poly-methyl-methacrylate (PMMA) layer was spin coated in a two-step process, consisting of a 5 second pre-spin step at 500 revolutions per minute (RPM), with an acceleration rate of 500 RPM s^{-1}, followed by a second spin step at 2500 RPM at an acceleration rate of 2000 RPM s^{-1}, again baked for 15 minutes at 180 °C and allowed to cool to room temperature. Following the same procedure a 950 k molecular weight A1 (1% in anisole) PMMA solution was coated with a 5000 RPM spin step, baked for 3 minutes and allowed to cool. Immediately before electron beam lithography (EBL) exposure, the substrate was spin coated with a proprietary conducting layer [DisCharge, DisChemInc] to mitigate against charge accumulation using the same procedure at 5000 RPM.

Electron beam exposure was performed with a Vistec EBPG 5000 at 100 kV accelerating voltage. To ensure shape fidelity of the ring-shaped patterns, a curved fracturing mode was used. The patterns were exposed at a 1400 μC cm^{-2} dose rate with a 3 nA current and a 300-micron aperture (approximately 6 nm spot size), along with a 4 nm beam step size. After exposure, the conducting polymer was removed by rinsing the substrate in DI water for 15 seconds, followed by immediate development for 90 seconds at 4 °C in chilled 4:1 ethanol:DI, during which the substrate was sonicated for 10 seconds.

Metal deposition was performed with an IntlVAC e-beam evaporator. First, a 2 nm chromium adhesion layer was deposited at a rate of 0.5 Å per second, followed by a 30 nm Au layer deposited at a rate of 0.1 Å per second at a pressure around 10^{-6} T.

The resist was removed by soaking the substrate overnight in acetone. The substrate was then cleaned in IPA, DI water and immediately dried with nitrogen gas.

FTIR measurements were conducted using a Bruker Lumos FTIR microscope, equipped with a liquid nitrogen-cooled mercury cadmium telluride (MCT) detector. Each spectrum was obtained by averaging 32 accumulations at a spectral resolution of 2 cm^{-1}. An aperture was employed to confine the measurement area to 120 μm × 120 μm, optimizing spatial resolution and focusing on the target region. The reflectance spectra were normalized against a gold reference, and atmospheric corrections were applied to account for the absorption of water vapor and CO_2.

To determine the resonance positions and quality factors (Q-factors), the reflectance dips were fitted with a Lorentzian line shape combined with a constant background. The Lorentzian function was defined as $L\ (\tilde{\nu}) = \frac{1}{1+(\frac{\tilde{\nu}-\tilde{\nu}_0}{\gamma})^2}$, where $\tilde{\nu}_0$ was the center frequency and γ was the half-width at half-maximum (HWHM). The FWHM was obtained as 2γ, and the Q-factor was subsequently calculated as $Q = \tilde{\nu}_0$ /FWHM.

Computational Details: The reflectance spectra were obtained through simulations using the MEEP software package.[28] The plasmonic arrays were arranged in a hexagonal pattern with a fixed pitch of 1000 nm for all simulations, except for the study shown in Figure 3A, where the pitch was varied between 800 nm and 1100 nm. The gold thickness of the plasmonic structures was kept constant at 50 nm. The dielectric function of gold was described with a Lorentz-Drude model with experimental data obtained from Rakić et al.,[29] which exhibit relatively higher intrinsic damping to other data sets and thus partially account for additional losses introduced by the Cr adhesion layer used in the experiments.[30,31] The dielectric function of silicon was set dispersionless with a value of $\epsilon_{Si} = 11.39$. A periodic boundary condition was used in all directions with an artificial absorber

layer at the end of the computational cell that was perpendicular to the plane of incidence of the incoming light and that blocked unwanted back reflections. Reflection spectra were normalized to a bare silicon surface.

Supporting Information

Supporting Information is available from the Wiley Online Library or from the author.

Acknowledgements

G.E.A. and L.P., contributed equally to this work. FDTD simulations were performed on the Spartan cluster maintained by the University of Melbourne This work was performed in part at the Melbourne Centre for Nanofabrication (MCN) and the Materials Characterization and Fabrication Platform (MCFP) at the University of Melbourne in the Victorian Node of the Australian National Fabrication Facility (ANFF) and the Bio21 Molecular Science & Biotechnology Institute (Ian Holmes Imaging Centre). The authors acknowledge funding support from the ANFF-Vic Technology Fellow Ambassador Program. They also thank the Australian Government for funding through the Centre of Excellence in Exciton Science (CE170100026). G.E.A. and L.P. gratefully acknowledge support from the Australian Government Research Training Program (RTP) Scholarship. J.A.H. thanks the Australian Research Council for support through the Future Fellowship scheme (FT180100295). G.E.A. further extends thanks for the support provided by the Dr. Albert Shimmins Postgraduate Writing-Up Award. The authors thank Dr. Michael Stuiber from MCN for his assistance on EBL patterning and fruitful discussions.

Conflict of Interest

The authors declare no conflict of interest.

Data Availability Statement

The data that support the findings of this study are openly available in MINERVA at https://minerva-elements.unimelb.edu.au/, 9999.

Keywords

FDTD simulations, metasurfaces, optical encoding, plasmon, plasmonic hybridization

Received: January 5, 2025
Revised: May 6, 2025
Published online: June 13, 2025

[1] J. Lafait, S. Berthier, C. Andraud, V. Reillon, J. Boulenguez, *Compt. Rendus Phys.* **2009**, *10*, 649.
[2] Y. Wang, E. W. Plummer, K. Kempa, *Adv. Phys.* **2011**, *60*, 799.
[3] K. Kumar, H. Duan, R. S. Hegde, S. C. W. Koh, J. N. Wei, J. K. W. Yang, *Nat. Nanotechnol.* **2012**, *7*, 557.
[4] X. Zhu, C. Vannahme, E. Højlund-Nielsen, N. A Mortensen, A. Kristensen, *Nat. Nanotechnol.* **2016**, *11*, 325.
[5] A. Kristensen, J. K. W. Yang, S. I. Bozhevolnyi, S. Link, P. Nordlander, N. J. Halas, N. A Mortensen, *Nat. Rev. Mater.* **2016**, *2*, 16088.
[6] H. Yang, K. Ou, H. Wan, Y. Hu, Z. Wei, H. Jia, X. Cheng, Na Liu, H. Duan, *Mater. Today* **2023**, *67*, 424.
[7] F. U. Richter, I. Sinev, S. Zhou, A. Leitis, S.-H. Oh, M. L. Tseng, Y. Kivshar, H. Altug, *Adv. Mater.* **2024**, *36*, 2314279.
[8] E. Panchenko, L. Wesemann, D. E. Gómez, T. D. James, T. J. Davis, A. Roberts, *Adv. Opt. Mater.* **2019**, *7*, 1900893.
[9] M-Su Ahn, J. Jeon, C. S. H. Hwang, D. S. Jeon, M. H. Kim, Ki-H Jeong, *Adv. Mater. Technol.* **2023**, *8*, 2201482.
[10] S. Rosas, K. A. Schoeller, E. Chang, H. Mei, M. A. Kats, K. W. Eliceiri, X. Zhao, F. Yesilkoy, *Adv. Mater.* **2023**, *35*, 2301208.
[11] H. Zhou, D. Li, Z. Ren, C. Xu, L-Fa Wang, C. Lee, *Sci. Adv.* **2024**, *10*, ado3179.
[12] D. Franklin, S. Modak, A. Vázquez-Guardado, A. Safaei, D. Chanda, *Light: Sci. Appl.* **2018**, *7*, 93.
[13] J. Lee, H. Lee, Y. J. Kim, Y. J. Yoo, S. Chang, G. J. Lee, J. H. Ko, K. M. Kang, D. Chanda, Y. M. Song, *Adv. Opt. Mater.* **2021**, 9.
[14] J. Cai, C. Zhang, W.-D. Li, *Adv. Opt. Mater.* **2021**, *9*, 2001401.
[15] T. Chen, B. M. Reinhard, *Adv. Mater.* **2016**, *28*, 3522.
[16] E. Heydari, J. R. Sperling, S. L. Neale, A. W. Clark, *Adv. Funct. Mater.* **2017**, *27*, 1701866.
[17] Z. Li, A. W. Clark, J. M. Cooper, *ACS Nano* **2016**, *10*, 492.
[18] Y. Sonnefraud, N. Verellen, H. Sobhani, G. A. E. Vandenbosch, V. V. Moshchalkov, P. Van Dorpe, P. Nordlander, S. A. Maier, *ACS Nano* **2010**, *4*, 1664.
[19] F. Hao, P. Nordlander, Y. Sonnefraud, P. V. Dorpe, S. A. Maier, *ACS Nano* **2009**, *3*, 643.
[20] A. E. Cetin, H. Altug, *ACS Nano* **2012**, *6*, 9989.
[21] P. Nordlander, E. Prodan, *Nano Lett.* **2004**, *4*, 2209.
[22] T. S. Neuman, C. Huck, J. Vogt, F. Neubrech, R. Hillenbrand, J. Aizpurua, A. Pucci, *J. Phys. Chem. C* **2015**, *119*, 26652.
[23] G. E. Akinoglu, J. A. Hutchison, *ACS Appl. Opt. Mater.* **2023**, *1*, 771.
[24] V. G. Kravets, A. V. Kabashin, W. L. Barnes, A. N. Grigorenko, *Chem. Rev.* **2018**, *118*, 5912.
[25] D. Barchiesi, S. Kessentini, N. Guillot, M. L. de la Chapelle, T. Grosges, *Opt. Express* **2013**, *21*, 2245.
[26] G. E. Akinoglu, E. M. Akinoglu, K. Kempa, M. Giersig, *Opt. Express* **2019**, *27*, 22939.
[27] H. Zhu, Q. Li, C. Tao, Yu Hong, Z. Xu, W. Shen, S. Kaur, P. Ghosh, M. Qiu, *Nat. Commun.* **2021**, *12*, 1805.
[28] A. F. Oskooi, D. Roundy, M. Ibanescu, P. Bermel, J. D. Joannopoulos, S. G. Johnson, *Comput. Phys. Commun.* **2010**, *181*, 687.
[29] A. D. Rakic, A. B. Djurisic, J. M. Elazar, M. L. Majewski, *Appl. Opt.* **1998**, *37*, 5271.
[30] F. Colas, D. Barchiesi, S. Kessentini, T. Toury, M. L. D. L. Chapelle, *J. Opt.* **2015**, *17*, 114010.
[31] H. S. Sehmi, W. Langbein, E. A. Muljarov, *Phys. Rev. B* **2017**, *95*, 115444.